INTERNATIONAL JOURNAL OF FLUID POWER, 2016
VOL. 17, NO. 1, 49–64
http://dx.doi.org/10.1080/14399776.2015.1127724

ServoFlight: pneumatically actuated full flight simulator

Justin Pradipta and Oliver Sawodny

Institute for System Dynamics, University of Stuttgart, Stuttgart, Germany

ABSTRACT

This contribution covers a new way to provide motion feedback in a full flight simulator. Seven pneumatic cylinders are utilized to actuate our 6 degrees-of-freedom motion platform. The motion platform being investigated is a parallel manipulator configured similarly to a Stewart platform with additional one redundant cylinder in the middle. The models of the pneumatic cylinder and the parallel manipulator are used to derive a dual control method. The dual control follows two different trajectories which are generated by a modified motion cueing algorithm and a force trajectory generator. The measurements are conducted on a full size build. The experiment results show that the platform performs well with a low total transport delay, therefore the platform is suitable to be used in a full flight simulator.

ARTICLE HISTORY
Received 14 August 2015
Accepted 27 November 2015

KEYWORDS
Pneumatic cylinder; parallel robot; motion platform; full flight simulator

1. Introduction

A flight simulator is a safe environment to familiarize a trainee into piloting before one steps into a real aircraft. They are broadly used in various applications from civilian airliners to military fighter planes. There are many benefits to train pilots in a flight simulator such as financial, time and most importantly safety (Allerton 2009).

The purpose of a flight simulator is to train pilot in procedure, system knowledge, radio communications and navigation skills. To support the purpose, the flight simulation has to be as close as possible to a real aircraft and the flying experience. At the same time, a high-fidelity flight simulator that facilitates such trainings can be very expensive. To address the cost problem, a new approach to provide a high fidelity flight simulator with affordable cost has to be investigated.

One of the major expenses in a full flight simulator (FFS) is the motion platform. The most common motion platforms for air or land vehicle simulators are parallel manipulators in hexapod configuration, commonly known as the Stewart platform. As the actuator in the manipulator, usually six hydraulic stamps or electro mechanics linear motors are used. The hydraulic/electro-mechanics hexapods are widely deployed at the pilot Type-Rating training facilities worldwide such as Airbus (2015), CAE (2015), Lufthansa Flight Training (2015) and Thales (2015).

As a new less expensive approach, the use of pneumatic actuators can be the solution (Wang *et al.* 1999). Pneumatic actuators are broadly used in automated manufacturing processes, but in the case of heavy-load motion platforms they are still not widely applied. Pneumatic actuators use pressurized air as their working medium, which makes their stiffness significantly lower and the effects of disturbances more present, emphasizing the importance of a precise and high-dynamic control arises (Hildebrandt *et al.* 2010).

Research on pneumatically actuated motion platforms, especially for a large motion platform is not broadly found as the research on the control design of pneumatic actuators itself. Most pneumatically driven parallel manipulators are used for direct human interaction, due to the compliant nature of pneumatic actuators (Gattringer *et al.* 2009). For instance, pneumatically actuated Stewart platform as a rehabilitation device can be found in Takaiwa (2010) and Girone *et al.* (2001). On the other hand, the compliant nature of pneumatic actuators is not a desirable characteristic for the motion platform of a simulator application. However, with a good control strategy this challenge can be dealt with. To overcome the problem, Pradipta *et al.* (2013) proposed a novel configuration for a six degrees-of-freedom (DoF) manipulator. The authors used seven pneumatic cylinder to increase the Stewart platform stiffness and its dynamic reserve in lifting heavy payloads.

The application of pneumatic cylinders in a driving simulator can be found in Andrievsky *et al.* (2014). They proposed a sliding-mode controller to control the Stewart platform. Although the controller is only tested in simulation so far, the method promises a good result with the real platform. Another attempt to control

CONTACT Justin Pradipta justin.pradipta@isys.uni-stuttgart.de

pneumatic cylinders in a Stewart platform was carried out in Grewal *et al.* (2011) on miniature scale. They successfully designed a Linear Quadratic Gaussian control to control the parallel manipulator, and showed that the controller is robust against disturbances.

The use of nonlinear control for a pneumatic actuator is proven to be a better solution as supported by Brun *et al.* (1999). They tried several methods of linear and nonlinear control and concluded that the nonlinear control performs significantly better for the pneumatic control. Bone and Ning (2007) compared two position-control schemes of sliding mode control (SMC); the first one was based on a linearized plant model and the second one was based on the non-linear system description. They achieved a slight improvement by using the more complicated non-linear model. Hildebrandt *et al.* (2010) utilized an input/output linearization method and applied nonlinear state feedback control for a pneumatic drive to follow a position trajectory. They emphasize the importance of the correct pneumatic drive sizing for the desired positioning task. Feedback linearization with regard to valve restriction was researched by Bigras *et al.* (2002). They used linear matrix inequities to calculate the controller gain and achieved a good control performance. SMC is a frequently used controller design method. Ning and Bone (2005) compared the SMC to a velocity/acceleration feedback plus feed-forward controller and prefer the SMC's slightly better performance. (Chen *et al.* (2009) utilized an integral sliding mode controller with multi-variable parameters and achieved improvement over a standard PID controller. An approach using nonlinear state dependent Riccati equation (SDRE) was done by Weickgenannt *et al.* (2010). They proposed a two DoF controller with a SDRE combined with a feedforward loop. A nonlinear control design approach for a pneumatic cylinder using Immersion and Invariance (I&I) method was done by Rapp *et al.* (2012a). They applied the I&I to design a robust controller with adaptive and robust tracking against unknown parameters. In the robust control front, Wang *et al.* (2001) carried out a study to model the pneumatic cylinder as a nonlinear system and design a robust controller based on the nonlinear system description. Meng *et al.* (2013) proposed an integrated direct/indirect adaptive robust control combining a robust control law and recursive least squares estimator to overcome the time variant parameter uncertainties in the pneumatic cylinder. Novel control design approaches, such as neural networks, are also found. Gross and Rattan (1997) trained multilayer neural networks to model the nonlinearity of the pneumatic cylinder and utilized it in a feed-forward loop to help a linear feedback controller; they obtained an acceptable performance result. Carniero and de Almeida (2011) used a neural-network based model combined with a nonlinear state feedback controller and achieve an improvement over a linear PID controller. A pragmatic approach was taken by Wang *et al.* (1999). They applied a modified PID controller and achieved decent stability performance by using the cylinder acceleration as a feedback.

Pneumatic actuators can be set to follow force trajectories as well. An exact input/output linearization method for force control was proposed by Rapp *et al.* (2012b), proving that pneumatic cylinders can follow a force trajectory very well. Ilchmann *et al.* (2006) derived a model of a pneumatic cylinder and designed a feedback force-controller using a practical proportional controller with saturation. They argued that the control strategy is effective, which is helped by the boundedness of the pneumatic actuator dynamics. Jang (2005) tried to control a pneumatic cylinder to follow position and force trajectories simultaneously using a non-interacting controller and a disturbance observer based on a nonlinear system model, he achieved good performance in both position and force tracking. Shen and Goldfarb (2007) designed a pneumatic actuator system that was simultaneously force and stiffness controlled by using two proportional valves. They designed a sliding model controller to achieve both objectives.

In this paper the pneumatically actuated FFS will be presented along with a detailed description of each component that makes the whole system. This contribution is based on the previous publications of the authors Pradipta *et al.* (2013) and Pradipta *et al.* (2015) with additions to the overall flight simulator performance analysis. The supporting measurement data will be presented as well.

2. Pneumatically actuated motion platform

In this section, the models of the platform and the pneumatic cylinder will be derived. The models derived will be used later for the control design and trajectory planning.

2.1. Overall system architecture

The FFS system begins with a flight simulation server, as described by Figure 1, which computes the dynamics of the simulated aircraft. It includes the aerodynamic model, engine model, gear model, and the environment where the aircraft is situated. Simultaneously, the corresponding graphics are generated and projected onto a 200° surround screen. A Diamond Simulation D-SIM-42 (Diamond Simulation 2015) is used for the flight simulator and is classified by the FAA as a flight training device (FAA 2008). The D-SIM-42 is only a FTD because it lacks of motion feedback. By adding a motion platform to provide a motion feedback, the system can be upgraded into a FFS. The Diamond D-SIM-42 specifically simulates the DA42 from Diamond Aircraft.

Next to the simulation computer is the motion cueing algorithm (MCA) which acts as a bridge between the simulated aircraft dynamics and the platform dynamics.

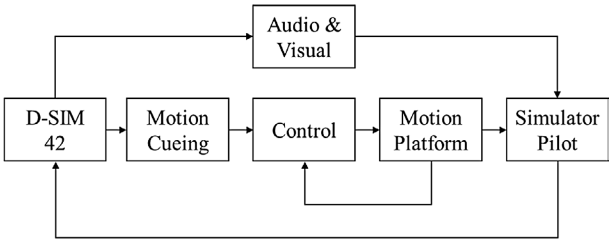

Figure 1. Full flight simulator system overview.

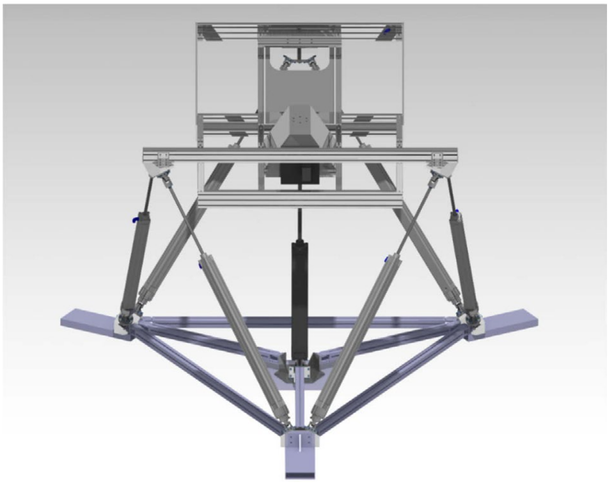

Figure 2. CAD rendering of the pneumatically actuated motion platform.

The MCA is necessary because an aircraft can fly limitlessly in the air while the platform is tethered to the ground. The MCA translates the simulator output into a motion that can stimulate the pilot's senses within feasible motion boundaries of the platform. The effect of motion feedback, if it is done correctly, can improve the simulator's performance by giving extra information during the simulated flights (Telban and Cardullo 2005).

The signals generated by the MCA are transformed into the actuator coordinate system and fed to the controller as a reference trajectory. Pneumatic cylinders are used as the actuators and a joint-space controller scheme is used to control the actuators in the parallel manipulator configuration (Siciliano *et al.* 2009). With this scheme there are seven decentralised controllers for each cylinder in the platform. The computer drawing of the motion platform can be seen in Figure 2.

The FFS system ends with a pilot as he receives the motion feedback provided by the platform and audio–visual information generated by the D-SIM-42. The pilot can then react properly according to the information, thus completing the loop of the simulator system.

2.2. The ServoFlight platform

The pneumatically-actuated seven-cylinder motion platform at the Institute for System Dynamic, University of Stuttgart (ServoFlight platform) was previously introduced in Pradipta *et al.* (2013). The pneumatic cylinders were chosen to make the motion platform more cost efficient compared to hydraulic or electro-mechanic actuators in the same configuration. The seven-cylinder construction was proposed to overcome the limited power output of the pneumatic cylinders.

The pneumatic cylinders in the platform are supplied with pressurized air at 8 bar. At the given pressure the six outer cylinders can exert force up to 2441 N and the middle cylinder can exert up to 9817 N (FESTO, 2015). The cylinders are equipped with an incremental position encoder with 0.01 mm resolution, and pressure sensors on every chamber. The motion envelope of the platform is presented in Table 1 (Figure 3).

The empty payload of the platform, in form of the simulator cockpit and the surround screen, is estimated at about 400 kg. With the known capability of the cylinders, the platform should have enough dynamic reserve to lift two average size pilots and perform the motion needed in a flight simulation (Pradipta *et al.* 2015).

2.3. Kinematics of the platform

The ServoFlight platform studied in this paper is configured similarly to a 3–3 Stewart platform. The top plate and the floor are connected by seven prismatic joints in parallel through three common mounting positions on the top plate and on the floor. On every top and bottom end of the cylinders is a spherical joint. The main difference to a normal Stewart platform is on the additional middle cylinder.

The platform has six DoF and is driven by seven prismatic actuators, this makes the manipulator fall into the domain of redundant actuation parallel manipulators (Merlet 2006). The middle cylinder becomes the redundant actuator in this manipulator. The advantage of a redundant configuration is an increase in manipulator end-effector stiffness with a trade-off to increased system complexity.

For kinematic modelling purposes, the middle cylinder will be omitted from the equation, because it tracks a force trajectory and is going to follow the motion of the platform along.

2.3.1. Inverse kinematic

The inverse kinematic transformation defines the relationship between the manipulator end-effector's position and the actuator position. The manipulator's six DoF are three translational motions $\boldsymbol{p}^B = \begin{bmatrix} x_p & y_p & z_p \end{bmatrix}$, and three rotational motions around three axes, known as roll, pitch and yaw, $\boldsymbol{\beta} = \begin{bmatrix} \Phi & \Theta & \Psi \end{bmatrix}$. The platform's position vector

$$\boldsymbol{x} = \begin{bmatrix} x_p & y_p & z_p & \Phi & \Theta & \Psi \end{bmatrix}^T \tag{1}$$

can be transformed into the cylinder lengths

$$\boldsymbol{q} = \begin{bmatrix} q_1, & \dots, & q_6 \end{bmatrix}^T, \tag{2}$$

Table 1. Platform translation and rotation limits.

Trans.	p [m]	$\dot{p}$ [m/s]	$\ddot{p}$ [m/s^2]	Rot.	β [°]	$\dot{\beta}$ [°/s]	$\ddot{\beta}$ [°/s^2]
x	−0.87, 1.15	±0.4	±2.9	Φ	±26	±28.6	±212
y	−0.97, 0.97	±0.3	±2.5	Θ	−15, 25	±25.7	±200
z	1.2, 1.85	±0.3	±2.5	Ψ	±20	±38.4	±441

Figure 3. Pneumatically actuated motion platform for a full flight simulator, "Project ServoFlight" at the Institute for System Dynamics, University of Stuttgart.

by using the inverse kinematic calculation into the cylinder lengths.

The transformation can be derived analytically by solving the geometric chain between the cylinder bottom end vector $\boldsymbol{b}_i^B$ and top end vector $\boldsymbol{c}_i^C$. A simplified drawing of the ServoFlight platform is depicted in Figure 4. The relation between the cylinder vector $\boldsymbol{l}_i$ and platform pose $\boldsymbol{x}$ can be written as

$$\boldsymbol{l}_i = \boldsymbol{p}^B + \boldsymbol{R}_{BC}\boldsymbol{c}_i^C - \boldsymbol{b}_i^B, \tag{3}$$

where $\boldsymbol{p}^B$ is the platform translational motion. $\boldsymbol{R}_{BC}$ is the combined rotation matrix between the rigid body coordinate system on the top plate C and the inertial coordinate system on the base B. The desired cylinder length can be found by returning the Euclidean distance of the cylinder vector $||\boldsymbol{l}_i||$.

$$\boldsymbol{R}_{BC}(\boldsymbol{\beta}) = \boldsymbol{R}_\Phi \boldsymbol{R}_\Theta \boldsymbol{R}_\Psi = \begin{bmatrix} c_\Theta c_\Psi & s_\Phi s_\Theta c_\Psi - c_\Phi s_\Psi & c_\Phi s_\Theta c_\Psi + s_\Phi s_\Psi \\ c_\Theta s_\Psi & s_\Phi s_\Theta s_\Psi + c_\Phi c_\Psi & c_\Phi s_\Theta s_\Psi - s_\Phi c_\Psi \\ -s_\Theta & s_\Phi c_\Theta & c_\Phi c_\Theta \end{bmatrix}. \tag{4}$$

2.3.2. *Direct kinematic*

The direct kinematic function is useful to translate the measured cylinder lengths $\boldsymbol{q}$ into the actual platform position $\boldsymbol{x}$. While the direct kinematic can be analytically solved, for every actuator length combination there are 40 possible solutions (Nielsen and Roth 1999). To obtain the manipulator position from the many possible solutions there is an elimination method, however it would be computationally demanding and unsuitable for a real time application (Tsai 1999).

Another way to solve the direct kinematic problem in a real-time environment is by solving it numerically (Merlet 2006). The Newton-Raphson iteration is used to solve the direct kinematic solution. The iteration can be written as

$$\boldsymbol{x}_{k+1} = \boldsymbol{x}_k - \boldsymbol{J}_x^{-1}\left(\boldsymbol{q}_k\left(\boldsymbol{x}_k\right) - \boldsymbol{q}_{meas}\right), \tag{5}$$

with a stopping criterion of $||\boldsymbol{q}_k(\boldsymbol{x}_k) - \boldsymbol{q}_{means}|| < \epsilon$, where ϵ is a chosen tolerance threshold. $\boldsymbol{J}_x \in \mathbb{R}^{6\times6}$ is the Jacobian matrix, which defines the relationship between the actuator velocities and the manipulator end-effector velocity

$$\dot{q}_i = \boldsymbol{n}_i \cdot \dot{\boldsymbol{p}}^B + (\boldsymbol{R}_{BC}\boldsymbol{c}_i^C \times \boldsymbol{n}_i) \cdot \dot{\boldsymbol{\beta}}. \tag{6}$$

Equation (6) can be written for the entire manipulator as $\dot{\boldsymbol{q}} = \boldsymbol{J}_x\dot{\boldsymbol{x}}$, where

$$\boldsymbol{J}_x = \begin{bmatrix} \boldsymbol{n}_1^T & [\boldsymbol{R}_{BC}\boldsymbol{c}_1^c \times \boldsymbol{n}_1]^T \\ \vdots & \vdots \\ \boldsymbol{n}_6^T & [\boldsymbol{R}_{BC}\boldsymbol{c}_6^c \times \boldsymbol{n}_6]^T \end{bmatrix}, \tag{7}$$

with $\boldsymbol{n}_i$ as the unit vector of the ith cylinder. It can be found by normalization of the cylinder defined by the following equation

$$\boldsymbol{n}_i = \frac{\boldsymbol{p}^B + \boldsymbol{R}_{BC}\boldsymbol{c}_i^C - \boldsymbol{b}_i^B}{||\boldsymbol{l}_i||}. \tag{8}$$

To guarantee the numerical solution synthesised by Equation (5) converges the Jacobian matrix $\boldsymbol{J}_x$ has to be of full rank. This is made possible by restricting the actuators' lengths to keep the platform within a safe workspace, thus avoiding singular configurations.

2.4. *Dynamic model of the platform*

The dynamic model of the platform is derived using the principle of virtual work (Tsai 1999). The dynamics of the manipulator are modelled through a virtual displacement of the general coordinate, in this case it

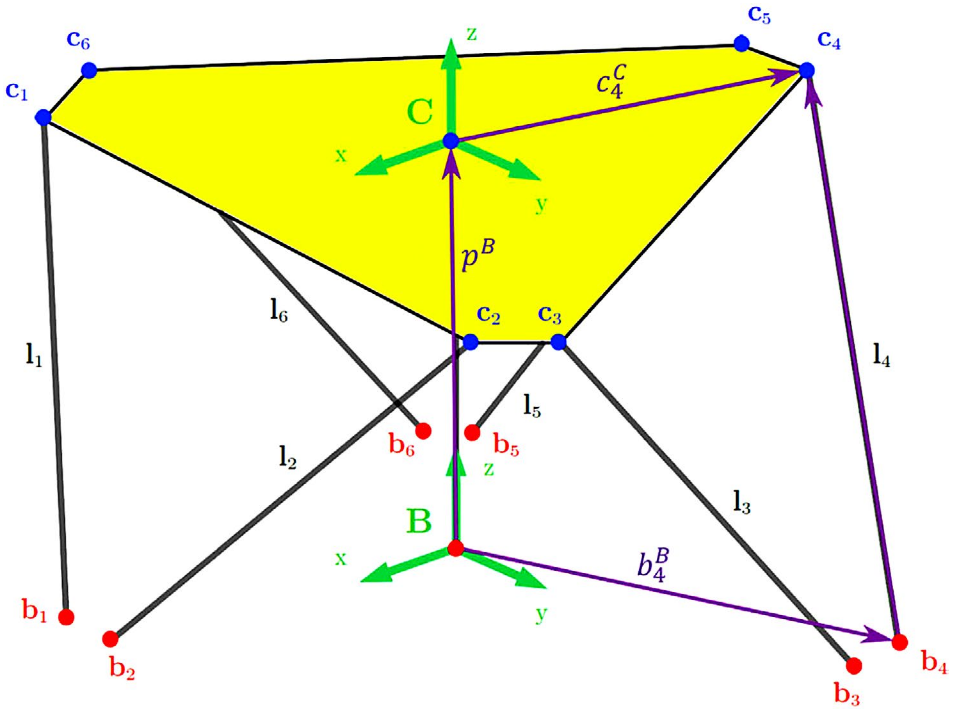

Figure 4. Simplified drawing of the ServoFlight platform with coordinate systems and vectors.

is the platform pose $\boldsymbol{x} \in \mathbb{R}^6$ in relation to the inertial coordinate B. To simplify the model, the dynamics of the actuators will be neglected. The equation of motion of the moving platform can be written as

$$\boldsymbol{M}(\boldsymbol{x})\ddot{\boldsymbol{x}} + \boldsymbol{C}(\boldsymbol{x}, \dot{\boldsymbol{x}}) + \boldsymbol{G} = \boldsymbol{J}_x^T(\boldsymbol{x})\boldsymbol{\tau}, \tag{9}$$

where $\boldsymbol{M}(\boldsymbol{x}) \in \mathbb{R}^{6\times 6}$ is a positive-definite generalized inertia matrix, $\boldsymbol{C}(\boldsymbol{x}, \dot{\boldsymbol{x}}) \in \mathbb{R}^6$ is the centrifugal and Coriolis term, $\boldsymbol{G}$ is the gravity vector, $\boldsymbol{J}_x$ is the Jacobian matrix of Equation (7), and $\boldsymbol{\tau} \in \mathbb{R}^6$ are the forces generated by the six outer cylinders in the direction of the cylinder stroke. Note that the model is defined at first without the redundant middle cylinder. The matrices in Equation (9) are given by

$$\boldsymbol{M}(\boldsymbol{x}) = \begin{bmatrix} \boldsymbol{m}_p & 0 \\ 0 & \boldsymbol{I}_P^B \end{bmatrix}, \tag{10}$$

$$\boldsymbol{C}(\boldsymbol{x}, \dot{\boldsymbol{x}}) = \begin{bmatrix} 0 \\ 0 \\ 0 \\ \boldsymbol{\omega} \times (\boldsymbol{I}_P^B \boldsymbol{\omega}) \end{bmatrix}, \tag{11}$$

$$\boldsymbol{G} = \begin{bmatrix} 0 & 0 & m_p g & 0 & 0 & 0 \end{bmatrix}. \tag{12}$$

2.5. Pneumatic cylinder model

The pneumatic cylinder model has to be derived as the base of the controller design. A pneumatic cylinder system consists of the pneumatic cylinder itself and a control valve. The control valve regulates the amount of air entering the cylinder with pressure p_v and the amount of air exhausted to the environment at atmospheric pressure p_0. The modelled pneumatic cylinder is a single rod pneumatic cylinder with effective area of A_1 and A_2 for the top and bottom chambers, respectively. The top chamber effective area A_1 is smaller due to the piston rod. For the model, the transport effect of the pneumatic tubing is neglected (Figure 5).

2.5.1. Cylinder dynamic

The cylinder equation of motion can be derived using Newton's second law, written as

$$M\ddot{q} = A_2 p_2 - A_1 p_1 - p_0\left(A_2 - A_1\right) - F_g - F_R, \tag{13}$$

To simplify the model a new variable K is introduced as

$$K = -p_0\left(A_2 - A_1\right) - F_g. \tag{14}$$

2.5.2. Chamber pressure dynamics

The model of the chamber pressure dynamics is based on the first law of thermodynamics. The pneumatic cylinder cambers are modelled as open systems and the process is assumed to be adiabatic with air as an ideal gas. The pressure dynamics in each chamber is

$$\dot{p}_j V_j + \kappa p_j \dot{V}_j = \kappa R T \dot{m}_j, \quad j = 1, 2. \tag{15}$$

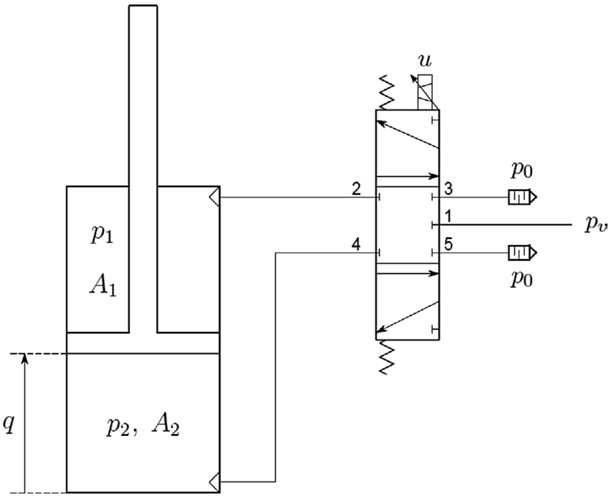

Figure 5. Pneumatic cylinder with a proportional directional control valve.

Solving Equation (15) for p yields

$$\dot{p}_1 = \frac{\kappa RT\dot{m}_1 + \kappa p_1 A_1 \dot{q}}{A_1\left(L_o + L - q\right)}, \tag{16}$$

and

$$\dot{p}_2 = \frac{\kappa RT\dot{m}_2 + \kappa p_2 A_2 \dot{q}}{A_2\left(L_o + q\right)}. \tag{17}$$

2.5.3. *Valve model*

One proportional directional control valve is used to regulate the air flow, thus supplying one cylinder chamber means exhausting the other chamber. The amount of mass flow through the valve opening is dictated by the valve spool input u. The mass flow equation is based on the work of (Rapp *et al.* 2012b). They identified the valve constant C_{mn} of the same valve used in the ServoFlight platform. The mass flow equation is written as

$$\dot{m}_1 = \tilde{u}\varphi\left(p_1\right), \tag{18}$$

and

$$\dot{m}_2 = \tilde{u}\varphi\left(p_2\right), \tag{19}$$

where the variable φ is defined by

$$\varphi(p_j) = \begin{cases} -\hat{C}\rho_0 p_v \psi\left(\frac{p_j}{p_v}, b\right) & \text{for} \quad u < 0, \\ -\hat{C}\rho_0 p_j \psi\left(\frac{p_0}{p_j}, b\right) & \text{for} \quad u > 0, \\ 0 & \text{for} \quad u = 0. \end{cases} \tag{20}$$

The term $\tilde{u}$ is the transformed input necessary to model the system into an input-affine formulation, where

$$\tilde{u} = \begin{cases} -C_{12}(u) = -C_{45}(u) & \text{for} \quad u < 0, \\ C_{23}(u) = C_{45}(u) & \text{for} \quad u > 0, \\ 0 & \text{for} \quad u = 0. \end{cases} \tag{21}$$

C_{mn} is the identified valve conductance value between port m and n. Additionally, ψ is defined by

$$\psi\left(\frac{p_b}{p_a}, b\right) = \begin{cases} 1, & \frac{p_b}{p_a} \leq b, \\ \sqrt{1 - \frac{\left(\frac{p_b}{p_a} - b\right)^2}{(1-b)^2}} & \frac{p_b}{p_a} \leq b. \end{cases} \tag{22}$$

to model the transition between subcritical and supercritical flows.

2.5.4. *State space representation*

The model of the pneumatic cylinder is summarized in a state space representation by defining the state vector

$$\breve{x} = [\ q \quad \dot{q} \quad p_1 \quad p_2\ ]^T. \tag{23}$$

The system dynamics are written in an input affine formulation

$$\dot{\breve{x}} = \boldsymbol{f}(\breve{x}) + \boldsymbol{g}(\breve{x})\breve{u}, \quad \breve{x}(0) = \breve{x}_0, \tag{24}$$

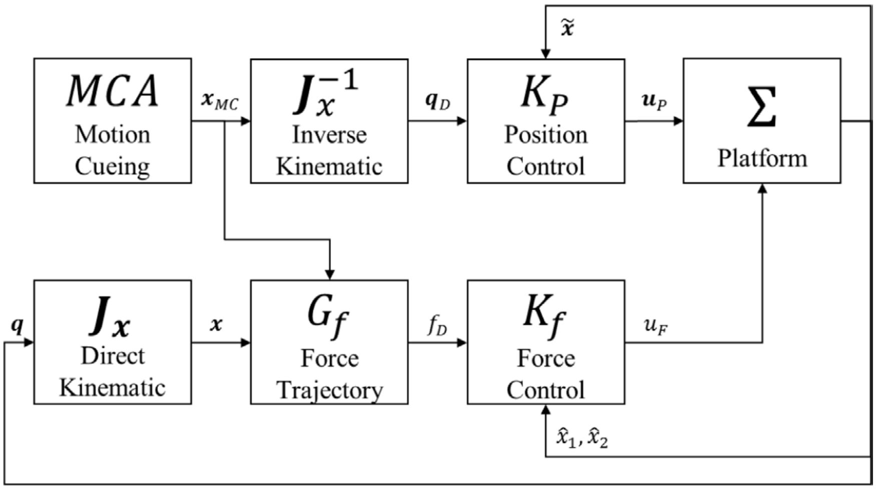

Figure 6. ServoFlight platform control strategy diagram.

with the measurement vector

$$\boldsymbol{y}_{meas} = [\check{x}_1 \quad \check{x}_2 \quad \check{x}_3 \quad \check{x}_4]^T, \tag{25}$$

where

Following Weickgenannt *et al.* (2010), a new state is introduced to reduce the model order, thus making the system differentially flat. The new state is the cylinder force

$$\boldsymbol{f}(\check{\boldsymbol{x}}) = \begin{bmatrix} \check{x}_2 \\ \frac{1}{M}(A_2\check{x}_4 - A_1\check{x}_3 + K - F_R) \\ \frac{k\check{x}_2\check{x}_3}{(L_0 + L - \check{x}_1)} \\ \frac{k\check{x}_2\check{x}_4}{(L_0 + \check{x}_1)} \end{bmatrix}, \quad \boldsymbol{g}(\check{x}) \begin{bmatrix} 0 \\ 0 \\ \frac{kRT\varphi_1(\check{x}_3)}{(L_0 + L - \check{x}_1)} \\ \frac{kRT\varphi_2(\check{x}_4)}{(L_0 + \check{x}_1)} \end{bmatrix}. \tag{26}$$

$$\tilde{x}_3 = F_{cyl} = A_2p_2 - A_1p_1. \tag{27}$$

Its dynamics depend on both of the cylinder pressures, written as

$$\dot{\tilde{x}}_3 = \dot{F}_{cyl} = A_2\dot{p}_2 - A_1\dot{p}_1. \tag{28}$$

By defining a state vector as $\tilde{\boldsymbol{x}} = [q \quad \dot{q} \quad F_{cyl}]^T$, a new input-affine state space representation of order of three can be written as

$$\dot{\tilde{\boldsymbol{x}}} = \tilde{\boldsymbol{f}}(\tilde{\boldsymbol{x}}) + \tilde{\boldsymbol{g}}(\tilde{\boldsymbol{x}})\tilde{u}, \quad \tilde{\boldsymbol{x}}(0) = \tilde{\boldsymbol{x}}_0, \tag{29}$$

with

$$\tilde{\boldsymbol{f}}(\tilde{x}) = \begin{bmatrix} \tilde{\boldsymbol{x}}_2 \\ \frac{1}{M}(\tilde{x}_3 + k - F_R) \\ -\kappa\tilde{x}_2(\frac{A_2p_2}{L_0 + \tilde{x}_1} + \frac{A_1p_1}{L_0 + L - \tilde{x}_1}) \end{bmatrix}, \tag{30}$$

$$\tilde{\boldsymbol{g}}(\tilde{\boldsymbol{x}}) = \begin{bmatrix} 0 \\ 0 \\ kRT\left(\frac{\varphi_2(p_2)}{L_0 + \tilde{x}_1} - \frac{\varphi_1(p_1)}{L_0 + L - \tilde{x}_1}\right) \end{bmatrix}, \tag{31}$$

and

$$\boldsymbol{y}_{est} = [\tilde{x}_1 \quad \tilde{x}_2 \quad \tilde{x}_3]^T. \tag{32}$$

In the new system model the chamber pressures are now time variant parameters, this should not be a problem because chamber pressures are measured by pressure sensors. The cylinder position and velocity can be measured. The cylinder force is estimated by Equation (27) using the measured cylinder chamber pressures. The model presented in Equation (29) will be used later in the outer cylinder position control design.

3. ServoFlight platform control

The ServoFlight platform is a redundant manipulator and in a redundant manipulator antagonistic forces can occur (Chakarov 2004). Antagonistic forces occur when several actuators are working against each other causing tension on the manipulator structure. To avoid antagonistic forces a dual control strategy is applied. The redundant middle cylinder will be a force controlled actuator and only the outer six cylinders will follow position trajectories. With this strategy the antagonistic force caused by the redundant cylinder can be minimized, provided that the middle cylinder is given a proper force trajectory.

Both controllers are going to use the trajectory generated by the MCA $\boldsymbol{x}_{MC}$, however, before the reference signal is fed into the controllers two transformation are necessary. An inverse kinematic is needed for the position control and a force trajectory generator is needed for the force controller. The control signal $\boldsymbol{u}_p$ is for the six outer cylinder positions and the control signal u_F is for the middle cylinder force (Figure 6).

3.2. Outer cylinder position control

The position tracking control of the outer cylinders is designed by using the I&I method proposed by Astolfi and Karagiannis (2008). The nonlinear control strategy utilizing the I&I method for a pneumatic cylinder was presented in Rapp *et al.* (2012a). A lower order asymptotically stable linear system is chosen to be the target system. The target system of order of two is written as

$$\dot{\xi} = \boldsymbol{\alpha}(\xi, \tilde{v}) = \begin{bmatrix} 0 & 1 \\ -\mu_1 & -\mu_2 \end{bmatrix}\xi + \begin{bmatrix} 0 \\ 1 \end{bmatrix}\tilde{v}. \tag{33}$$

A globally attractive manifold is defined to map the original system onto the target system

$$\phi(\tilde{\boldsymbol{x}}, \tilde{v}) = \tilde{x}_3 - M\left(\tilde{v} - \mu_1\tilde{x}_1 - \mu_2\tilde{x}_2\right) + K - F_R, \tag{34}$$

where $\phi(\tilde{\boldsymbol{x}}, \tilde{v}) = 0$, makes $\tilde{x}_3 = M\left(\tilde{v} - \mu_1\tilde{x}_1 - \mu_2\tilde{x}_2\right) - K + F_R$.The system is supposed to track the desired trajectory

$$y^* = \xi_1^* = \tilde{x}_1^*, \tag{35}$$

$$\dot{y}^* = \xi_2^* = \tilde{x}_2^*, \tag{36}$$

$$\tilde{v} = \dot{\xi}_2^* + \mu_1\xi_1^* + \mu_2\xi_2^* = \dot{\tilde{x}}_2^* + \mu_2\tilde{x}_2^* + \mu_1\tilde{x}_1^*. \tag{37}$$

The control law is derived from the manifold dynamics

$$\dot{\zeta} = \left(\frac{\partial \phi}{\partial \tilde{\boldsymbol{x}}}\right)^T (\boldsymbol{f}_0(\tilde{\boldsymbol{x}}) + \boldsymbol{f}_1(\tilde{\boldsymbol{x}})\boldsymbol{\theta} + \boldsymbol{g}(\tilde{\boldsymbol{x}})v(\tilde{\boldsymbol{x}}, \boldsymbol{\theta})) + \frac{\partial \boldsymbol{\phi}}{\partial \tilde{v}}\dot{\tilde{v}} = -\lambda\zeta, \tag{38}$$

where $\boldsymbol{\theta}$ is the friction force in the cylinder F_R. The control law can be written as

$$\begin{aligned} u = v\left(\tilde{x}, F_R\right) = & \frac{-1}{\kappa RT\left(\frac{\varphi_2}{L_0 + \tilde{x}_1} - \frac{\varphi_1}{L_0 + L - \tilde{x}_1}\right)} \\ & \Big(\lambda(K - M(\tilde{v}^* - \mu_2\tilde{x}_2 - \mu_1\tilde{x}_1) + \tilde{x}_3 - F_R) \\ & - M\dot{\tilde{v}}^* + \mu_2\left(K + \tilde{x}_3 - F_R\right) + M\mu_1\tilde{x}_2 - \frac{\kappa p_2\tilde{x}_2A_2}{L_0 + \tilde{x}_1} \\ & - \frac{\kappa p_1\tilde{x}_2A_1}{L_0 + L - \tilde{x}_1}\Big), \end{aligned} \tag{39}$$

with $\lambda, \mu_1, \mu_2 > 0$ and

$$\dot{\tilde{v}}^* = \dots\tilde{x}_d + \mu_2\dots\tilde{x}_d + \mu_1\dot{\tilde{x}}_d, \quad \tilde{\boldsymbol{x}}_d \in \boldsymbol{C}^3. \tag{40}$$

$F_R = \widehat{F}_R - \sigma M\tilde{x}_2$, $\sigma > 0$ is the parameter update law, according to Rapp *et al.* (2012a) it is defined by

$$\dot{\widehat{F}}_R = \sigma\left(\tilde{x}_3 + K - \widehat{F}_R + \sigma M\widehat{x}_2\right). \tag{41}$$

3.3. Middle cylinder force control

Reduced system dynamics are utilized to design the force controller. With a new state vector $\hat{\boldsymbol{x}} = [p_1 \quad p_2]^T$, the state-space representation in input-affine formulation is given by

$$\dot{\hat{\boldsymbol{x}}} = \hat{\boldsymbol{f}}(\hat{\boldsymbol{x}}) + \hat{\boldsymbol{g}}(\hat{\boldsymbol{x}})\hat{u}, \quad \hat{\boldsymbol{x}}(0) = \hat{\boldsymbol{x}}_0, \tag{42}$$

$$\hat{y}_{ctrl} = h(\hat{\boldsymbol{x}}) = F_{cyl} = \hat{x}_2A_2 - \hat{x}_1A_1 - p_0\left(A_2 - A_1\right) \tag{43}$$

with

$$\hat{\boldsymbol{f}}(\hat{\boldsymbol{x}}) = \begin{bmatrix} \frac{\kappa\hat{x}_1\dot{q}}{L_0 + L - q} \\ \frac{\kappa\hat{x}_2\dot{q}}{L_0 + q} \end{bmatrix}, \quad \hat{\boldsymbol{g}}(\hat{\boldsymbol{x}}) = \begin{bmatrix} \frac{\kappa RT\varphi\left(\hat{x}_1\right)}{A_1\left(L_0 + L - q\right)} \\ \frac{\kappa RT\varphi\left(\hat{x}_2\right)}{A_2\left(L_0 + q\right)} \end{bmatrix}, \tag{44}$$

$$\hat{\boldsymbol{y}}_{meas} = \begin{bmatrix} \hat{x}_1 & \hat{x}_2 \end{bmatrix}^T. \tag{45}$$

Notice that the piston position q and velocity $\dot{q}$ become time-variant parameters, and the friction inside the middle cylinder is neglected. Exact input–output linearization is used to design the controller (Isidori 1995). The derived control law is written as

$$\hat{u} = \frac{-\mathcal{L}_f h(\hat{\boldsymbol{x}}) + \hat{v}}{\mathcal{L}_g h(\hat{\boldsymbol{x}})}, \tag{46}$$

where $\hat{v}$ is the new virtual input defined by

$$\hat{v} = \dot{F}_{ref} + K_P\left(F_{ref} - F\right) + K_I\int F_{ref} - F\mathrm{d}\tau \tag{47}$$

4. Trajectory generation

Due to the use of the dual control strategy which divides the task of positioning and weight lifting to the outer cylinders and the middle cylinder, respectively, two kinds of trajectories must be generated. The position trajectories of the outer cylinders are generated by the MCA. It uses the linear and angular accelerations computed by the flight simulator. The force trajectory for the middle cylinder is derived from the motion trajectory generated by the MCA.

4.1. Motion cueing algorithm

The MCA used in this paper consists of three channels: the translational acceleration channel, rotational accelerations channel, and the tilt coordination channel. The translation channel uses the linear acceleration of the aircraft $\ddot{\boldsymbol{p}}_A$ to generate the linear position trajectory of the platform $\boldsymbol{p}_s$ through a high pass filter and a series of integrators. The rotational channel uses the same principles as the linear channel but with the aircraft's rotational acceleration $\ddot{\boldsymbol{\beta}}_A$ to generate the platform desired rotation $\boldsymbol{\beta}_s$. The tilt coordination calculates the amount of additional platform rotation angle to simulate constant acceleration. The graphical representation of the MCA can be seen in Figure 7. The following subsections will explain every part of the MCA in more detail.

4.1.1. Nonlinear scaling and coordinate transformation

At first, the reference accelerations generated by the flight simulator computer have to be limited and scaled to ensure the generated motion by the algorithm can be realized by the platform. The scaling function is a third order polynomial that acts as a nonlinear gain (Telban and Cardullo 2005). The polynomial scaling for every n-channel is given by

$$x_{SL,n} = sign(x_{S,n})(c_{3,n}x_{S,n}^3 + c_{2,n}x_{S,n}^2 + c_{1,n}x_{s,n} + c_{0,n}) \tag{48}$$

The scaled input then has to be transformed from the aircraft's rigid body coordinate system into the platform inertial coordinate system. In the case of the translational channel, the transformation is done by using the combined rotation matrix given by Equation (4), where $\boldsymbol{R}_{IB} = \boldsymbol{R}_{BC}$.

To transform the rotational accelerations from the rigid body coordinate system of the aircraft into the inertial coordinate system of the platform, the following equation is used

$$\ddot{\boldsymbol{\beta}}_I = \dot{\boldsymbol{T}}_{IB} \cdot \dot{\boldsymbol{\beta}}_B + \boldsymbol{T}_{IB} \cdot \ddot{\boldsymbol{\beta}}_B, \tag{49}$$

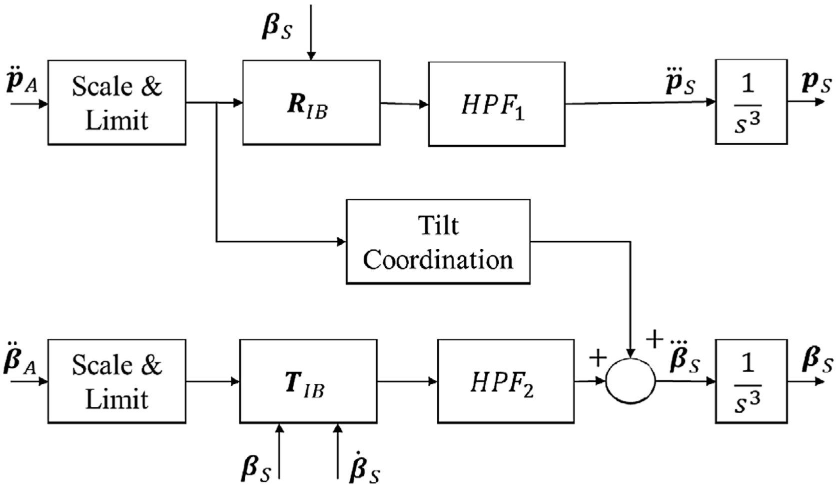

Figure 7. C^3 motion cueing algorithm.

where

$$\boldsymbol{T}_{IB}(\boldsymbol{\beta}) = \begin{bmatrix} 1 & s_\Phi \mathrm{t}_\Theta & c_\Phi t_\Theta \\ 0 & c_\Phi & -s_\Phi \\ 0 & \frac{s_\Phi}{c_\Theta} & \frac{c_\Phi}{c_\Theta} \end{bmatrix}, \tag{50}$$

and the derivative is

$$\dot{\boldsymbol{T}}_{IB}(\boldsymbol{\beta}, \dot{\boldsymbol{\beta}}) = \begin{bmatrix} 0 & s_\Phi\left(t_\Theta^2 + 1\right)\dot{\Theta} + c_\Phi t_\Theta \dot{\Phi} & c_\Phi\left(t_\Theta^2 + 1\right)\dot{\Theta} - s_\Phi t_\Theta \dot{\Phi} \\ 0 & -s_\Phi \dot{\Phi} & -c_\Phi \dot{\Phi} \\ 0 & \frac{c_\Phi \dot{\Phi}}{c_\Theta} + \frac{s_\Phi s_\Theta \dot{\Theta}}{c_\Theta^2} & \frac{c_\Phi s_\Theta \dot{\Theta}}{c_\Theta^2} - \frac{s_\Phi \dot{\Phi}}{c_\Theta} \end{bmatrix}. \tag{51}$$

4.1.2. High pass filters

From Equation (39) it is known that the controller requires the position trajectory to be three times continuously differentiable or $\boldsymbol{C}^3$, thus the use of a basic classical washout filter (Reid and Nahon 1986) is unsuitable since the signal generated by those filters are only $\boldsymbol{C}^2$. A way to solve this problem is by using higher order high-pass filters which are three times differentiable, e.g.

$$HPF_n = k_n \frac{s^3}{s^4 + 4\omega_n s^3 + 6\omega_n^2 s^2 + 4\omega_n^3 s + \omega_n^4}. \tag{52}$$

Both translational and rotational channels use a fourth order high pass filter. The filter parameters are tuned following the research of Fischer (2009). In his research he compares several MCAs and investigates methods to find the suitable parameters to give the most desirable simulator behaviour.

4.1.3. Tilt coordination

The tilt coordination channel has to be modified. In the classical MCA the tilt coordination cross channel is not included in the second derivative of the angle, making the derivate inconsistent.

The tilt coordination is usually approached by an inverse tangent equation to simulate the low frequency components of the accelerations through gravity. By tilting the simulator cabin the lateral acceleration can be simulated. The equations to find the angles are

$$\Phi_{TC} = \tan^{-1}\left(\frac{-a_{LP,y}}{g}\right) \approx \frac{-a_{LP,y}}{g}, \text{ and } \Theta_{TC} = \tan^{-1}\left(\frac{a_{LP,x}}{g}\right) \approx \frac{a_{LP,x}}{g}. \tag{53}$$

The tilt coordination instead will be approached by a third order high-pass filter. It is added into the angular channel as the third derivative of the tilt angle. The equation is written as

$$\mathrm{HPF}_{TCn} = \frac{k_{TCn}}{g} \frac{s^3}{s^3 + 3\omega_n s^2 + 3\omega_n^2 s + \omega_n^3}. \tag{54}$$

The tilt coordination signal generated by Equation (54) will be integrated three times along with the output from the high-pass filter of the rotational channel. Being a third order high-pass filter, the third integration will leave an offset. If it is tuned correctly, the end result will be similar to the output of an already familiar tilt coordination given by Equation (53).

4.1.4. Transformation into actuator coordinates

To transform the desired position trajectory from Cartesian coordinates into the cylinder lengths the inverse kinematic calculation given in Equation (3) can be used. However, to transform the derivatives the following equations should be used;

$$\dot{\boldsymbol{q}}_D = \boldsymbol{J}_x(\boldsymbol{x}_{MC})\dot{\boldsymbol{x}}_{MC}, \tag{55}$$

$$\ddot{\boldsymbol{q}}_D = \dot{\boldsymbol{J}}_x\left(\boldsymbol{x}_{MC}, \dot{\boldsymbol{x}}_{MC}\right)\dot{\boldsymbol{x}}_{MC} + \boldsymbol{J}_x\left(\boldsymbol{x}_{MC}\right)\ddot{\boldsymbol{x}}_{MC}, \tag{56}$$

$$\ddot{\boldsymbol{q}}_D = \ddot{\boldsymbol{J}}_x\left(\boldsymbol{x}_{MC}, \dot{\boldsymbol{x}}_{MC}, \ddot{\boldsymbol{x}}_{MC}\right)\dot{\boldsymbol{x}}_{MC} + 2(\dot{\boldsymbol{J}}_x(\boldsymbol{x}_{MC}, \dot{\boldsymbol{x}}_{MC})\ddot{\boldsymbol{x}}_{MC}) + \boldsymbol{J}_x\left(\boldsymbol{x}_{MC}\right)\dddot{\boldsymbol{x}}_{MC}, \tag{57}$$

where $\boldsymbol{q}_D = \begin{bmatrix} q_{D,1} & \cdots & q_{D,6} \end{bmatrix}^T$ and $\boldsymbol{x}_{MC} = \begin{bmatrix} \boldsymbol{p}_S & \boldsymbol{\beta}_S \end{bmatrix}^T \in \mathbb{R}^6$or the six DoF of the Cartesian coordinate. $\boldsymbol{J}_x$ is the Jacobian matrix given by Equation (6), and the derivative of the Jacobian is defined by

$$\dot{\boldsymbol{J}}_x\left(\boldsymbol{x}, \dot{\boldsymbol{x}}, \boldsymbol{q}, \dot{\boldsymbol{q}}\right) = \begin{bmatrix} \dot{\boldsymbol{n}}_1^T & \frac{\mathrm{d}}{\mathrm{d}t}\left[\boldsymbol{R}_{BC}\boldsymbol{c}_1^C \times \boldsymbol{n}_1\right]^T \\ \vdots & \vdots \\ \dot{\boldsymbol{n}}_6^T & \frac{\mathrm{d}}{\mathrm{d}t}\left[\boldsymbol{R}_{BC}\boldsymbol{c}_1^C \times \boldsymbol{n}_1\right]^T \end{bmatrix}, \tag{58}$$

where

$$\dot{\boldsymbol{n}}_i = \frac{q_i\left(\dot{\boldsymbol{p}}^B + \dot{\boldsymbol{R}}_{BC}\boldsymbol{c}_i^C\right) - \dot{q}_i\left(\boldsymbol{p}^B + \boldsymbol{R}_{BC}\boldsymbol{c}_i^C - \boldsymbol{b}_i^B\right)}{q_i^2}. \tag{59}$$

The derivative of the combined rotation matrix $\dot{\boldsymbol{R}}_{BC}\left(\boldsymbol{\beta}, \dot{\boldsymbol{\beta}}\right) \in \mathbb{R}^{3\times3}$, the detailed derivation can be seen in Appendix. The cylinder velocities $\dot{\boldsymbol{q}}_D = \begin{bmatrix} \dot{q}_{D,1} & \cdots & \dot{q}_{D,6} \end{bmatrix}^T$ are obtained by Equation (55) and the time derivative of the rotational part is

$$\frac{\mathrm{d}}{\mathrm{d}t}\left[\boldsymbol{R}_{BC}\boldsymbol{c}_i^C \times \boldsymbol{n}_i\right] = \dot{\boldsymbol{R}}_{BC}\boldsymbol{c}_i^C \times \boldsymbol{n}_i + \boldsymbol{R}_{BC}\boldsymbol{c}_i^C \times \dot{\boldsymbol{n}}_i. \tag{60}$$

The second derivative of the Jacobian is given by

$$\ddot{\boldsymbol{J}}_x\left(\boldsymbol{x}, \dot{\boldsymbol{x}}, \ddot{\boldsymbol{x}}, \boldsymbol{q}, \dot{\boldsymbol{q}}, \ddot{\boldsymbol{q}}\right) = \begin{bmatrix} \ddot{\boldsymbol{n}}_1^T & \frac{\mathrm{d}^2}{\mathrm{d}t^2}\left[\boldsymbol{R}_{BC}\boldsymbol{c}_1^C \times \boldsymbol{n}_1\right]^T \\ \vdots & \vdots \\ \ddot{\boldsymbol{n}}_6^T & \frac{\mathrm{d}^2}{\mathrm{d}t^2}\left[\boldsymbol{R}_{BC}\boldsymbol{c}_1^C \times \boldsymbol{n}_1\right]^T \end{bmatrix}, \tag{61}$$

where

$$\ddot{\boldsymbol{n}}_i = \frac{1}{q_i^4}\left[q_i^2\left(q_i\left(\ddot{\boldsymbol{p}}^B + \ddot{\boldsymbol{R}}_{BC}\boldsymbol{c}_i^C\right) - \ddot{q}_i\left(\boldsymbol{p}^B + \boldsymbol{R}_{BC}\boldsymbol{c}_i^C - \boldsymbol{b}_i^B\right)\right) - 2q_i\dot{q}_i\left(q_i\left(\dot{\boldsymbol{p}}^B + \dot{\boldsymbol{R}}_{BC}\boldsymbol{c}_i^C\right) - \dot{q}_i\left(\boldsymbol{p}^B + \boldsymbol{R}_{BC}\boldsymbol{c}_i^C - \boldsymbol{b}_i^B\right)\right)\right], \tag{62}$$

and

$$\frac{\mathrm{d}^2}{\mathrm{d}t^2}\left[\boldsymbol{R}_{BC}\boldsymbol{c}_i^C \times \boldsymbol{n}_i\right] = \ddot{\boldsymbol{R}}_{BC}\boldsymbol{c}_i^C| \times \boldsymbol{n}_i + 2\left(\dot{\boldsymbol{R}}_{BC}\boldsymbol{c}_i^C \times \dot{\boldsymbol{n}}_i\right) + \boldsymbol{R}_{BC}\boldsymbol{c}_i^C \times \ddot{\boldsymbol{n}}_i. \tag{63}$$

The elements of the second derivative of the combined rotational matrix $\ddot{\boldsymbol{R}}_{BC}\left(\boldsymbol{\beta}, \dot{\boldsymbol{\beta}}, \ddot{\boldsymbol{\beta}}\right) \in \mathbb{R}^{3\times3}$ can be found in the appendix. The cylinder accelerations $\ddot{\boldsymbol{q}}_D = \begin{bmatrix} \ddot{q}_{D,1} & \cdots & \ddot{q}_{D,6} \end{bmatrix}^T$ are obtained by the equation (56).

4.2. Middle cylinder force trajectory generation

To harness the benefit of the redundant configuration the middle cylinder needs a sensible force trajectory. The force trajectory is calculated using the dynamic model derived in Section 2.2. The dynamic model is extended by introducing the middle cylinder into the equation defined by

$$\boldsymbol{f}_{mid} = f_{mid}\frac{\boldsymbol{p}}{\|\boldsymbol{p}\|}. \tag{64}$$

Defining a new force vector

$$\tilde{\boldsymbol{\tau}} = [\tau_1, \quad \ldots, \quad \tau_6, \quad f_{mid}]^T \in \mathbb{R}^7, \tag{65}$$

yields a new dynamic model

$$\boldsymbol{M}(\boldsymbol{x})\ddot{\boldsymbol{x}} + \boldsymbol{C}(\boldsymbol{x}, \dot{\boldsymbol{x}}) + \boldsymbol{G} = \begin{bmatrix} \boldsymbol{J}_x^T(\boldsymbol{x}) & \begin{bmatrix} \hat{\boldsymbol{p}} \\ 0 \end{bmatrix} \end{bmatrix}\tilde{\boldsymbol{\tau}}. \tag{66}$$

The updated Jacobian matrix becomes irregular; to obtain the desired cylinder force $\tilde{\boldsymbol{\tau}}$, the pseudoinverse method can be used. However, following the author's previous contribution (Pradipta *et al.* 2015), an assumption can be made such that

$$\hat{\boldsymbol{p}}^T\boldsymbol{L}(\boldsymbol{x})\boldsymbol{\tau} = 0. \tag{67}$$

The forces generated by the outer cylinders that point in the same direction as the middle cylinder should be compensated by the middle cylinder. With

$$\boldsymbol{L}(\boldsymbol{x}) = \begin{bmatrix} \boldsymbol{n}_1, & \ldots, & \boldsymbol{n}_6 \end{bmatrix} \tag{68}$$

as the unit vector of the outer cylinders, the new platform dynamic equation becomes

$$\begin{bmatrix} M(\boldsymbol{x})\ddot{\boldsymbol{x}} \\ 0 \end{bmatrix} + \begin{bmatrix} \boldsymbol{C}(\boldsymbol{x}, \dot{\boldsymbol{x}}) \\ 0 \end{bmatrix} + \begin{bmatrix} \boldsymbol{G} \\ 0 \end{bmatrix} = \underbrace{\begin{bmatrix} \boldsymbol{J}_x^T\boldsymbol{x} & \begin{bmatrix} \hat{\boldsymbol{p}} \\ 0 \end{bmatrix} \\ \hat{\boldsymbol{p}}^T\boldsymbol{L}\boldsymbol{x} & 0 \end{bmatrix}}_{\mathbf{Q}(\boldsymbol{x})}\tilde{\boldsymbol{\tau}}. \tag{69}$$

The desired cylinder force can be obtained by solving Equation (69) for $\tilde{\boldsymbol{\tau}}$.

$$\tilde{\boldsymbol{\tau}}(\boldsymbol{x}, \boldsymbol{x}_{MC}, \dot{\boldsymbol{x}}_{MC}, \ddot{\boldsymbol{x}}_{MC}) = \boldsymbol{Q}^{-1}(\boldsymbol{x}) \left[\left(\begin{matrix} M(\boldsymbol{x})\ddot{\boldsymbol{x}} \\ 0 \end{matrix}\right] + \begin{bmatrix} \boldsymbol{C}(\boldsymbol{x}, \dot{\boldsymbol{x}}) \\ 0 \end{bmatrix} + \begin{bmatrix} \boldsymbol{G} \\ 0 \end{bmatrix}\right). \tag{70}$$

Note that the desired middle cylinder force is a function of the desired position trajectories and the actual platform position. This measure is taken to guarantee that the $\boldsymbol{Q}(\boldsymbol{x})$ matrix will not become singular if the desired platform position is unfeasible.

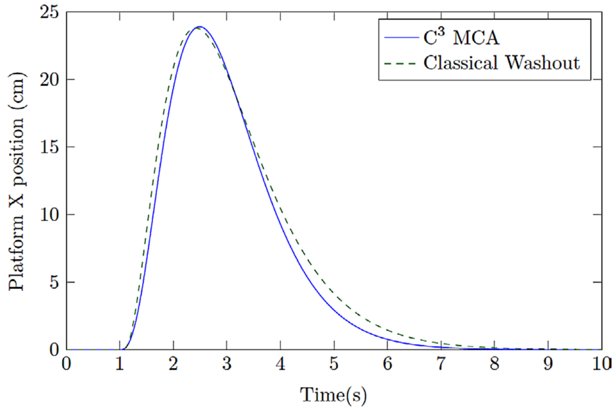

Figure 8. Comparison of the filter responses.

5. Measurement results

To see if the platform is suitable for a flight simulator application. Experiments were conducted to measure the controller performances and the platform's overall response to the pilot input.

5.1. MCA latency

The use of the higher order high pass filter is necessary to create a three times differentiable trajectory for the controller. However, the higher order filter is going to introduce additional time delay to the MCA. To estimate the additional time delay a unit step acceleration signal is fed into the high pass filter, timed at the one second. From the simulation, the delay can reach up to 30 ms. The behaviour of this MCA is, as expected, similar to a classical washout filter (Figure 8).

The delay introduced by the MCA is going to be the total introduced delay of the trajectory generation system. This can be achieved by the omission of the intermediate C^3 trajectory generator that would normally have to be used, as it would introduce additional delay.

5.2. Controller performance

To test the position controller performance, the platform is set to follow a desired roll trajectory of 10° in 2.5 s, which is a representative reference trajectory since the output from the washout filter is about the same motion rate. From the measurements, the platform can follow the desired trajectory with small deviation. The maximum deviation during the test is 0.3° on the roll angle. Due to the coupled nature of the manipulator, a motion on one degree-of-freedom will affect the rest of the DoF. However, the platform shows only small deviations on the other DoF, as shown in Figure 9. On the actuator level, those deviations translate into a maximum of 1 cm on the actuator coordinate, as shown in Figure 10. Nevertheless, the platform induces a small

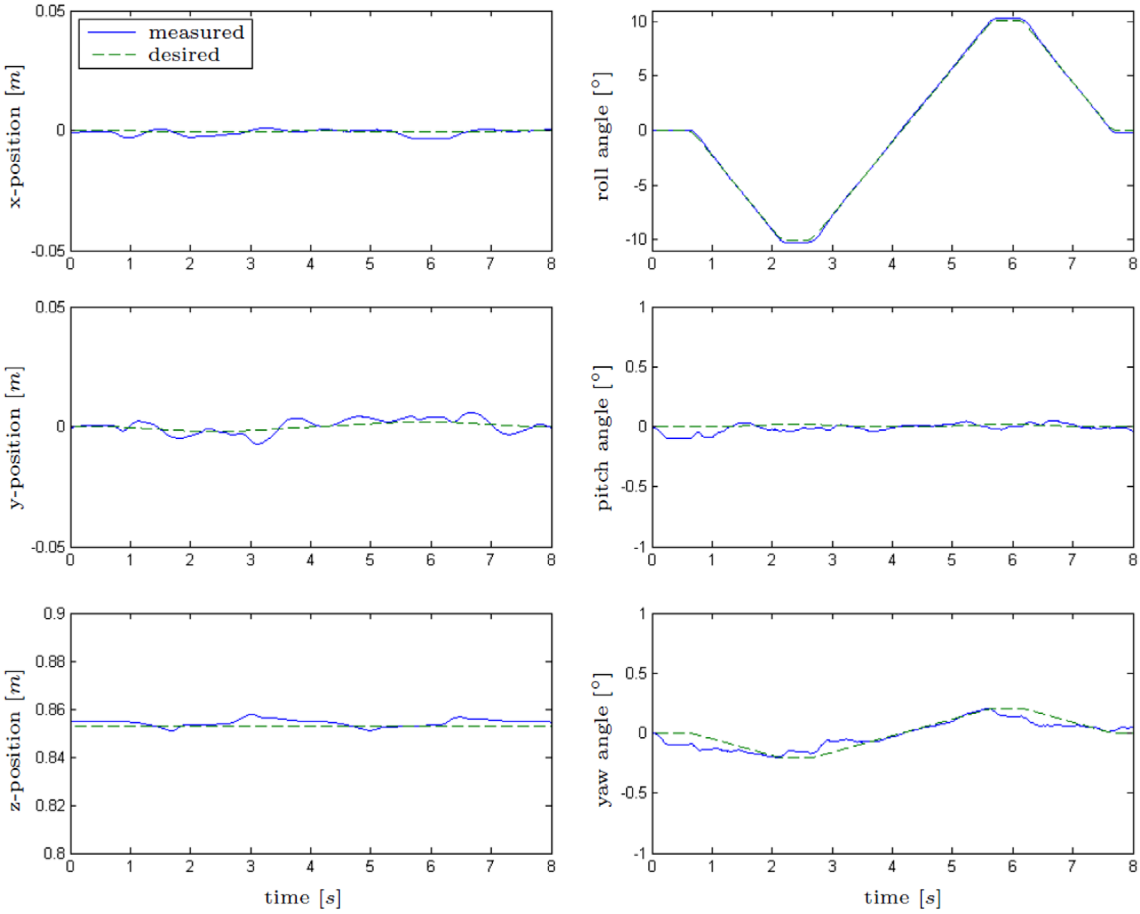

Figure 9. Position tracking performance of the platform.

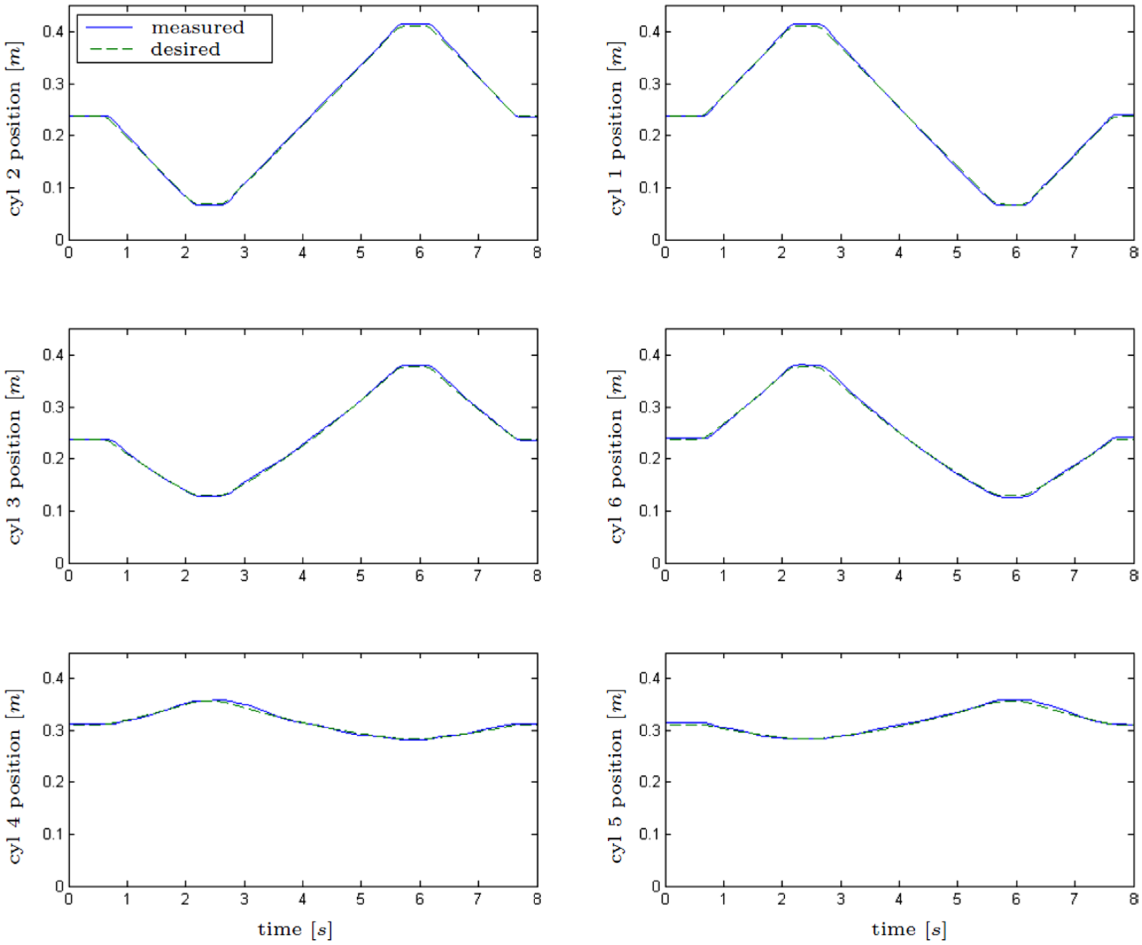

Figure 10. Actuators position tracking performance.

time delay during the motion, measured about 60 ms from the beginning of the motion. This delay is visualized by Figure 11, which is a blown out view of the platform roll angle.

The force controller performs similarly well. It follows the desired force trajectory with a maximum deviation of 10 N, which is very small. The deviation of the force tracking performance does not affect the overall platform performance significantly since a fraction of the payload weight is still able to be lifted by the outer cylinders (Figure 12).

Overall, the performance of the controllers can be considered good considering the use of the compliant pneumatic actuators. The most important thing is that the platform can react to rapid changes in trajectory to provide well timed motion cues. This will be investigated in the next section, where the total latency of the system is tested.

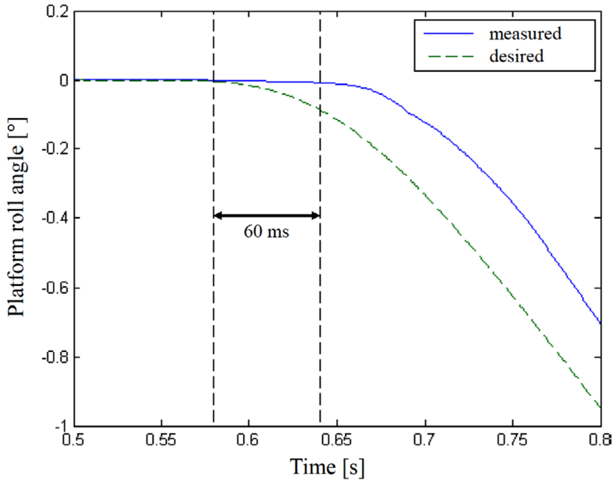

Figure 11. Platform motion deviation, zoomed in view of the platform roll angle.

5.3. Overall system performance

To test whether the platform is suitable to be used as a motion simulator or not. The reaction time of the system will be measured. The International Civil Aviation Organization (ICAO) states in their Manual (ICAO, 2009) that the maximum total transport delay for a motion simulator must be lower than 150 ms. The delay is measured from the moment of flight control input to the time of platform motion (Figure 13).

To measure the transport delay in the platform an experiment involving a pilot is conducted. The pilot pulls the joystick towards him as quick as possible, and consequently the platform should pitch backwards (positive pitch). Please note that the joystick input does not exactly scale directly to the platform motion because the signal must go through the aerodynamic simulator

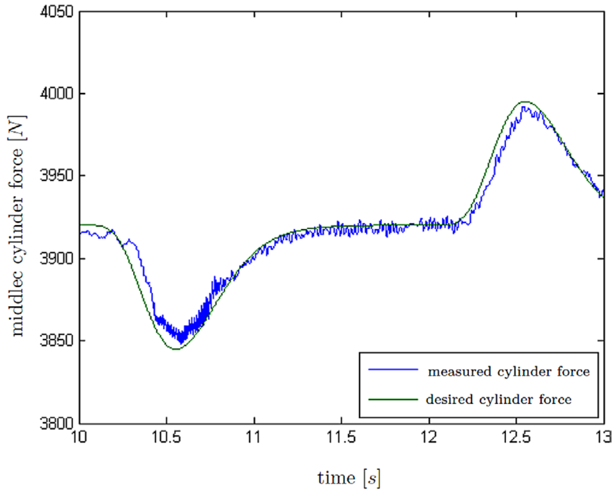

Figure 12. Middle cylinder force tracking performance.

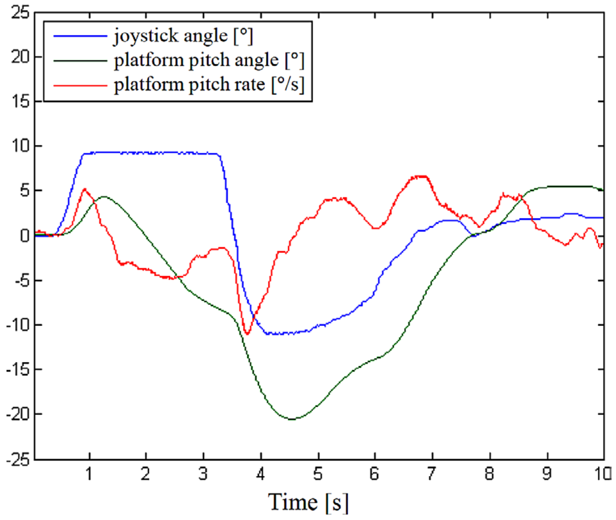

Figure 14. The motion simulator response to pilots input.

of the airplane and then the MCA. Therefore, the test is only to determine the amount of time between the input and the platform reaction.

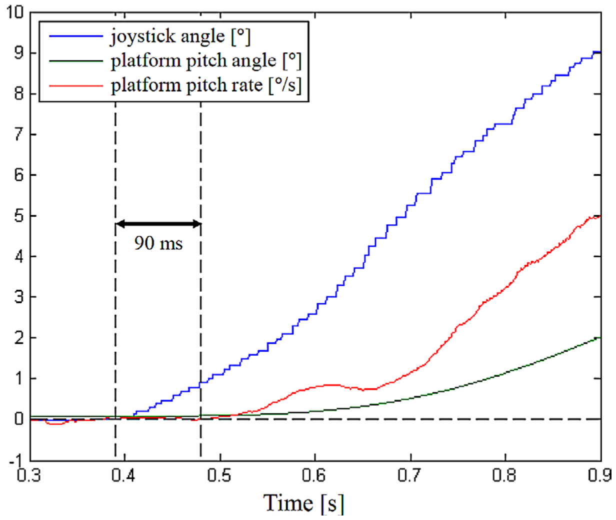

Figure 15. Measured total transport delay of the flight simulator.

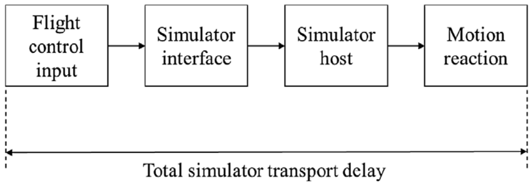

Figure 13. Total transport delay (ICAO, 2009).

From the experiment, the time between the pilot's input and the platform reaction, the total transport delay, is measured at 90 ms. The measured time is lower than the ICAO standard maximum of 150 ms. This reaction time is critical to creating well timed motion feedback and avoiding false cues that can cause motion sickness. The result of this experiment is depicted in Figure 14, and zoomed in to the critical moment in Figure 15.

6. Conclusion

The utilization of a redundantly actuated motion platform driven by seven pneumatic cylinders for a FFS application is proven to be feasible. The platform can follow the reference position and force trajectories generated by the MCA and the force trajectory generator, respectively, with considerably small deviation. The most important property of a motion platform is the overall system latency and from the experiment the platform response is still within the ICAO specified maximum delay.

Nomenclature

A_j	Piston effective area of chamber *j*
$\hat{C}$	Valve conductance scaling factor
C_{mn}	Identified valve constant
F_R	Cylinder friction
F_{cyl}	Cylinder force
F_g	Force of gravity
L_0	Cylinder dead length
$\dot{m}_j$	Mass flow of chamber *j*
m_p	Platform weight
p_0	Atmospheric pressure
p_j	Pressure in chamber *j*
p_v	Supply pressure
$\ddot{q}_i$	Cylinder number *i* acceleration
q_i	Cylinder number *i* velocity
q_i	Cylinder number *i* position
$\tilde{u}$	Transformed control signal for cylinder position
$\hat{u}$	Control signal for cylinder force
V_j	Cylinder chamber *j* volume
x_p	Platform *x* position
y_p	Platform *y* position
z_p	Platform *z* position
$\boldsymbol{b}_i^B$	Cylinder bottom mounting coordinate
$\boldsymbol{c}_i^C$	Cylinder top mounting coordinate
$\boldsymbol{I}_p^B \in \mathbb{R}^{3\times3}$	Platform inertia matrix
$\boldsymbol{J}_x$	Jacobian matrix
$\boldsymbol{l}_i$	Cylinder vector

$\boldsymbol{m}_p \in \mathbb{R}^{3\times3}$	Platform mass matrix
$\boldsymbol{n}_i$	Cylinder unit vector
$\boldsymbol{p}_B \in \mathbb{R}^3$	Platform translation vector
$\boldsymbol{R}_{BC}$	Combined rotation matrix
ρ_0	Air density
$\mathcal{L}$	Lie derivative
Θ	Platform pitch angle
Φ	Platform roll angle
Ψ	Platform yaw angle
L	Cylinder maximum length
R	Specific gas constant
T	Absolute temperature
g	Gravity
u	Control signal
$\boldsymbol{C}(\boldsymbol{x}, \dot{\boldsymbol{x}}) \in \mathbb{R}^6$	Coriolis vector
$\boldsymbol{G} \in \mathbb{R}^6$	Gravity vector
$\boldsymbol{M}(\boldsymbol{x}) \in \mathbb{R}^{6\times6}$	Platform generalized inertia matrix
$\boldsymbol{q} \in \mathbb{R}^6$	Cylinder lengths vector
$\boldsymbol{x} \in \mathbb{R}^6$	Platform pose vector
κ	Isentropic exponent
$\boldsymbol{\beta} \in \mathbb{R}^3$	Platform rotational angle vector
$\boldsymbol{\omega} \in \mathbb{R}^3$	Platform angular velocity vector

Disclosure statement

No potential conflict of interest was reported by the authors.

Notes on contributors

Justin Pradipta received the bachelor and master degrees in engineering physics from the Bandung Institute of Technology, Indonesia, in 2007 and 2010 respectively. He joined the Institute for System Dynamics at the University of Stuttgart in 2011 with a DAADscholarship and is working toward his Ph.D. His research interests include control engineering, mechatronic systems, and trajectory generation.

Oliver Sawodny received the diploma degree in electrical engineering from the University of Karlsruhe, Germany, in 1991, and the Ph.D. degree from the University of Ulm, Germany, in 1996. In 2002, he became a full professor at the Technical University of Ilmenau, and in 2005, he became the Director of the Institute for System Dynamics at the University of Stuttgart. His current research interests include methods of differential geometry, trajectory generation, methods and application to mechatronic systems.

ORCID

Justin Pradipta http://orcid.org/0000-0001-6419-3823

References

Airbus, 2015. *FLIGHT TRAINING WITH A350 XWB* [online]. Available from: http://www.airbus.com/support/training/flight/flight-training-with-a350-xwb/ [Accessed 1 November 2015].

Allerton, D., 2009. *Principles of flight simulation*. Chichester: John Wiley & Sons.

Andrievsky, B., Kazunin, D., Kostygova, D., and Kuznetsov, N., 2014. Control of pneumatically actuated 6-DOF Stewart. *In*: *19th International conference on methods and models in automation and robotics (MMAR)*, Miedzyzdroje, 663–668.

Astolfi, A. and Karagiannis, D., 2008. *Nonlinear and adaptive control with applications*. London: Springer Verlag.

Bigras, P., Khayati, K., and Wong, T., 2002. Modified feedback linearization controller for pneumatic system with non negligible connection port restriction. *In*: *IEEE International conference on systems, man and cybernetics*, Yasmine Hammamet, Tunisia, 227–231.

Bone, G. and Ning, S., 2007. Experimental comparison of position tracking control algorithms for pneumatic cylinder actuators. *IEEE/ASME transaction on mechatronics*, 12, 557–561.

Brun, X., *et al.*, 1999. Control of an electropneumatic actuator, comparison between some linear and nonlinear control laws. *Journal of systems and control engineering*, 213, 387–403.

CAE, 2015. *CAE 7000XR SERIES LEVEL D FULL-FLIGHT SIMULATOR* [online]. Available from: http://www.cae.com/civil-aviation/simulation-products/cae-7000XR-series-full-flight-simulator/ [Accessed 1 November 2015].

Carniero, J.F. and de Almeida, F.G., 2011. A high-accuracy trajectory following controller for pneumatic devices. *International Journal of Advance Manufacturing Technology*, 253–267.

Chakarov, D., 2004. Study of the antagonistic stiffness of parallel manipulators with actuation redundancy. *Mechanism and machine theory*, 39, 589–601.

Chen, H.-M., Chen, Z.-Y., & Chung, M.-C., 2009. Implementation of an integral sliding mode controller for a pneumatic cylinder position servo control system. *In*: *Fourth international conference on innovative computing, information and control*, Kaohsiung, 552–555.

Diamond Simulation, 2015. *D-SIM-42* [online]. Available from: http://www.diamond-simulation.de/d-sim-42.html?&L=3 [Accessed 15 May 2015].

FAA, 2008. *14 CFR part 60, NSP consolidated version* [online]. Available from: www.faa.gov/about/initiatives/nsp/media/consolidated_version.pdf [Accessed 12 May 2015].

FESTO, 2015. *Standard cylinders DNCI, with measuring transducer DADE, Standard cylinder DNC 15552* [online]. Available from: www.festo.com/catalog [Accessed 1 July 2015].

Fischer, M., 2009. *Motion-Cueing-Algortihmen für eine realitätsnahe Bewegungssimulation* [Motion Cueing Algorithms for a near reality motion simulation]. s.l.: Deutsches Zentrum für Luft- und Raumfahrt.

Gattringer, H., Naderer, R., and Bremer, H., 2009. Modeling and control of a pneumatically driven stewart platform. *In*: H. Ulbrich and L. Ginzinger, eds. *Motion and vibration control*. s.l. Springer, 93–102.

Girone, M., *et al.*, 2001. A Stewart platform-based system for ankle telerehabilitation. *Autonomous robots*, 10, 203–212.

Grewal, K., Dixon, R., and Pearson, J., 2011. Control design for a pneumatically actuated parallel link manipulator. *21st International conference on systems engineering (ICSEng)*, Las Vegas, NV, 43–48.

Gross, D.C. and Rattan, K.S., 1997. A feedforward MNN controller for pneumatic cylinder trajectory tracking control. *International conference on neural networks*, Houston, TX, 794–799.

Hildebrandt, A., Neumann, R., and Sawodny, O., 2010. Optimal system design of SISO-servopneumatic positioning drives. *IEEE transactions on control systems technology*, 18 (1), 35–44.

ICAO, 2009. *Manual of criteria for the qualification of flight simulation training devices, volume I – aeroplanes*. 3rd ed. Montréal, Quebec: International Civil Aviation Organization.

Ilchmann, A., Sawodny, O., and Trenn, S., 2006. Pneumatic cylinders: modelling and feedback force-control. *International journal of control*, 650–661.

Isidori, A., 1995. *Nonlinear control systems*. London: Springer Verlag.

Jang, J.-S., 2005. Simultaneous trajectory tracking control of position and force with pneumatic cylinder driving apparatus. *Journal of mechanical science and technology*, 1107–1115.

Lufthansa Flight Training, 2015. *Full Flight Simulators* [online]. Available from: www.lufthansa-flight-training.com [Accessed 1 November 2015].

Meng, D., Tao, G. and Zhu, X., 2013. Integrated direct/indirect adaptive robust motion trajectory tracking control of pneumatic cylinders. *International journal of control*, 1620–1633.

Merlet, J., 2006. *Parallel robots*. Dordrecht, The Netherlands: Springer.

Nielsen, J. and Roth, B., 1999. On the kinematic analysis of robotic mechanisms. *The international journal of robotics research*, 18 (12), 1147–1160.

Ning, S. and Bone, G.M., 2005. Experimental comparison of two pneumatic servo position control algorithms. *IEEE International Conference on Mechatronics and Automation*, 37–42.

Pradipta, J., K., K.L., & Sawodny, O., 2015. Force trajectory generation for the redundant actuator in a pneumatically actuated Stewart platform. *6th International conference on automation, robotics and applications (ICARA)*, pp. 525–530.

Pradipta, J., Klünder, M., Weickgenannt, M., and Sawodny, O., 2013. Development of a pneumatically driven flight simulator Stewart platform using motion and force control. *IEEE/ASME international conference on advanced intelligent mechatronics (AIM)*, 158–163.

Rapp, P., Klünder, M., Sawodny, O., and Tarin, C., 2012a. Nonlinear adaptive and tracking control of a pneumatic actuator via immersion and invariance. *51st IEEE conference on decision and control*, 4145–4151.

Rapp, P., Weickgenannt, M., Tarin, C., and Sawodny, O., 2012b. Valve flow rate identification and robust force control for a pneumatic actuator used in a flight simulator. *American control conference*, 1806–1813.

Reid, L. and Nahon, M., 1986. *Flight simulation motion-base drive algorithms: part II - selecting the system parameters. UTIAS Report No. 307*, s.l.: s.n.

Siciliano, B., Sciavicco, L., Villani, L. and Oriolo, G., 2009. *Robotics: modelling, planning and control*. London: Springer.

Shen, X. and Goldfarb, M., 2007. Simultaneous force and stiffness control of a pneumatic actuator. *Journal of dynamic systems, measurement, and control*, 425–434.

Takaiwa, M., 2010. Wrist rehabilitaion equipment using pneumatic parallel manipulator. *World Automation Congress (WAC)*, 1–6.

Telban, R. and Cardullo, F., 2005. *Motion cueing algorithm development: human-centered linear and nonlinear approaches*. New York, NY: NASA.

Thales, 2015. *Civil Training Solutions* [online]. Available from: https://www.thalesgroup.com/en/worldwide/aerospace/civil-training-solutions-0 [Accessed 1 November 2015].

Tsai, L., 1999. *Robot analysis: the mechanics of serial and parallel manipulators*. New York, NY: Wiley.

Wang, J., Pu, J., and Moore, P., 1999. A practical control strategy for servo-pneumatic actuator systems. *Control engineering practice*, 7, 1483–1488.

Wang, D.J.D., Pu, J., Moore, P., and Wang, J., 2001. Modelling study, analysis and robust servocontrol of pneumatic cylinder actuator systems. *IEE Proceedings - Control Theory and Applications*, 148 (1), 35–42.

Weickgenannt, M., Zimmert, N., Klumpp, S., and Sawodny, O., 2010. Application of SDRE control to servopneumatic drives. *IEEE international conference on control application*, 1725–1729.

Appendix

$$\dot{\boldsymbol{R}}_{BC}(1,1) = \dot{\Theta} s_\Theta c_\Psi - \dot{\Psi} c_\Theta s_\Psi \tag{71}$$

$$\dot{\boldsymbol{R}}_{BC}(1,2) = \dot{\Phi} s_\Phi s_\Psi - \dot{\Psi} c_\Phi c_\Psi + \dot{\Phi} c_\Phi s_\Theta c_\Psi + \dot{\Theta} s_\Phi c_\Theta c_\Psi - \dot{\Psi} s_\Phi s_\Theta s_\Psi \tag{72}$$

$$\dot{\boldsymbol{R}}_{BC}(1,3) = \dot{\Phi} c_\Phi s_\Psi + \dot{\Psi} s_\Phi c_\Psi + \dot{\Theta} c_\Phi c_\Theta c_\Psi - \dot{\Phi} s_\Phi s_\Theta c_\Psi - \dot{\Psi} c_\Phi s_\Theta s_\Psi \tag{73}$$

$$\dot{\boldsymbol{R}}_{BC}(2,1) = \dot{\Psi} c_\Theta c_\Psi - \dot{\Theta} s_\Theta s_\Psi \tag{74}$$

$$\dot{\boldsymbol{R}}_{BC}(2,2) = \dot{\Phi} c_\Phi s_\Theta s_\Psi - \dot{\Psi} c_\Phi s_\Psi - \dot{\Phi} s_\Phi c_\Psi + \dot{\Theta} s_\Phi c_\Theta s_\Psi + \dot{\Psi} s_\Phi s_\Theta c_\Psi \tag{75}$$

$$\dot{\boldsymbol{R}}_{BC}(2,3) = \dot{\Psi} s_\Phi s_\Psi - \dot{\Phi} c_\Phi c_\Psi + \dot{\Theta} c_\Phi c_\Theta s_\Psi + \dot{\Psi} c_\Phi s_\Theta c_\Psi - \dot{\Phi} s_\Phi s_\Theta s_\Psi \tag{76}$$

$$\dot{\boldsymbol{R}}_{BC}(3,1) = -\dot{\Theta} c_\Theta \tag{77}$$

$$\dot{\boldsymbol{R}}_{BC}(3,2) = \dot{\Phi} c_\Phi c_\Theta - \dot{\Theta} s_\Phi s_\Theta \tag{78}$$

$$\dot{\boldsymbol{R}}_{BC}(3,3) = -\dot{\Phi} s_\Phi c_\Theta - \dot{\Theta} c_\Phi s_\Theta \tag{79}$$

$$\ddot{\boldsymbol{R}}_{BC}(1,1) = 2 s_\Theta s_\Psi \dot{\Theta}\dot{\Psi} - c_\Theta c_\Psi \dot{\Psi}^2 - c_\Psi s_\Theta \ddot{\Theta} - c_\Theta s_\Psi \ddot{\Psi} - c_\Theta c_\Psi \dot{\Theta}^2 \tag{80}$$

$$\begin{aligned}\ddot{\boldsymbol{R}}_{BC}(1,2) = {} & c_\Phi s_\Psi \dot{\Phi}^2 + c_\Phi s_\Psi \dot{\Psi}^2 - c_\Phi c_\Psi \ddot{\Psi} + s_\Phi s_\Psi \ddot{\Phi} - c_\Psi s_\Phi s_\Theta \dot{\Phi}^2 \\ & - c_\Psi s_\Phi s_\Theta \dot{\Theta}^2 - c_\Psi s_\Phi s_\Theta \dot{\Psi}^2 + c_\Phi c_\Psi s_\Theta \ddot{\Phi} \\ & + c_\Theta c_\Psi s_\Phi \ddot{\Theta} + 2 c_\Psi s_\Phi \dot{\Phi}\dot{\Psi} - s_\Phi s_\Theta s_\Psi \ddot{\Psi} + 2 c_\Phi c_\Theta c_\Psi \dot{\Phi}\dot{\Theta} \\ & - 2 c_\Phi s_\Theta s_\Psi \dot{\Phi}\dot{\Psi} - 2 c_\Theta s_\Phi s_\Psi \dot{\Theta}\dot{\Psi}\end{aligned} \tag{81}$$

$$\begin{aligned}\ddot{\boldsymbol{R}}_{BC}(1,3) = {} & c_\Phi s_\Psi \ddot{\Phi} - s_\Phi s_\Psi \dot{\Psi}^2 - s_\Phi s_\Psi \dot{\Phi}^2 + c_\Psi s_\Phi \ddot{\Psi} \\ & - c_\Phi c_\Psi s_\Theta \dot{\Phi}^2 - c_\Phi c_\Psi s_\Theta \dot{\Theta}^2 - c_\Phi c_\Psi s_\Theta \dot{\Psi}^2 + c_\Phi c_\Theta c_\Psi \ddot{\Theta} \\ & + 2c_\Phi c_\Psi \dot{\Phi}\dot{\Psi} - c_\Psi s_\Phi s_\Theta \ddot{\Phi} - c_\Phi s_\Theta s_\Psi \ddot{\Psi} + 2 s_\Phi s_\Theta s_\Psi \dot{\Phi}\dot{\Psi} \\ & - 2c_\Theta c_\Psi s_\Phi \dot{\Phi}\dot{\Theta} - 2c_\Phi c_\Theta s_\Psi \dot{\Theta}\dot{\Psi}\end{aligned} \tag{82}$$

$$\ddot{\boldsymbol{R}}_{BC}(2,1) = c_\Theta c_\Psi \ddot{\Psi} - c_\Theta s_\Psi \dot{\Psi}^2 - c_\Theta s_\Psi \dot{\Theta}^2 - s_\Theta s_\Psi \ddot{\Theta} - 2c_\Psi s_\Theta \dot{\Theta}\dot{\Psi} \tag{83}$$

$$\begin{aligned}\ddot{\boldsymbol{R}}_{BC}(2,2) = {} & c_\Phi s_\Theta s_\Psi \ddot{\Phi} - c_\Phi c_\Psi \dot{\Psi}^2 - c_\Psi s_\Phi \ddot{\Phi} - c_\Phi s_\Psi \ddot{\Psi} \\ & - s_\Phi s_\Theta s_\Psi \dot{\Phi}^2 - s_\Phi s_\Theta s_\Psi \dot{\Theta}^2 - s_\Phi s_\Theta s_\Psi \dot{\Psi}^2 - c_\Phi c_\Psi \dot{\Phi}^2 \\ & + c_\Theta s_\Phi s_\Psi \ddot{\Theta} + 2 s_\Phi s_\Psi \dot{\Phi}\dot{\Psi} + c_\Psi s_\Phi s_\Theta \ddot{\Psi} \\ & + 2c_\Phi c_\Theta s_\Psi \dot{\Phi}\dot{\Theta} + 2c_\Phi c_\Psi s_\Theta \dot{\Phi}\dot{\Psi} + 2c_\Theta c_\Psi s_\Phi \dot{\Theta}\dot{\Psi}\end{aligned} \tag{84}$$

$$\begin{aligned}\ddot{\boldsymbol{R}}_{BC}(2,3) = {} & c_\Psi s_\Phi \dot{\Phi}^2 + c_\Psi s_\Phi \dot{\Psi}^2 - c_\Phi c_\Psi \ddot{\Phi} + s_\Phi s_\Psi \ddot{\Psi} \\ & - c_\Phi s_\Theta s_\Psi \dot{\Phi}^2 - c_\Phi s_\Theta s_\Psi \dot{\Theta}^2 - c_\Phi s_\Theta s_\Psi \dot{\Psi}^2 \\ & + c_\Phi c_\Theta s_\Psi \ddot{\Theta} + 2c_\Phi s_\Psi \dot{\Phi}\dot{\Psi} + c_\Phi c_\Psi s_\Theta \ddot{\Psi} - s_\Phi s_\Theta s_\Psi \ddot{\Phi} \\ & + 2c_\Phi c_\Theta c_\Psi \dot{\Theta}\dot{\Psi} - 2c_\Theta s_\Phi s_\Psi \dot{\Phi}\dot{\Theta} - 2c_\Psi s_\Phi s_\Theta \dot{\Phi}\dot{\Psi}\end{aligned} \tag{85}$$

$$\ddot{\boldsymbol{R}}_{BC}(3,1) = s_\Theta \dot{\Theta}^2 - c_\Theta \ddot{\Theta} \tag{86}$$

$$\ddot{\boldsymbol{R}}_{BC}(3,2) = c_\Phi c_\Theta \ddot{\Phi} - c_\Theta s_\Phi \dot{\Theta}^2 - c_\Theta s_\Phi \dot{\Phi}^2 - s_\Phi s_\Theta \ddot{\Theta} - 2c_\Phi s_\Theta \dot{\Phi}\dot{\Theta} \tag{87}$$

$$\ddot{\boldsymbol{R}}_{BC}(3,3) = 2 s_\Phi s_\Theta \dot{\Phi}\dot{\Theta} - c_\Phi c_\Theta \dot{\Theta}^2 - c_\Theta s_\Phi \ddot{\Phi} - c_\Phi s_\Theta \ddot{\Theta} - c_{text\Phi} c_\Theta \dot{\Phi}^2 \tag{88}$$